ELSEVIER

Physics Reports 337 (2000) 37–65

PHYSICS REPORTS

www.elsevier.com/locate/physrep

# Pattern forming instabilities of the nematic smectic-B interface

T. Tóth-Katona[a,*], T. Börzsönyi[a], Á. Buka[a], R. González-Cinca[b], L. Ramírez-Piscina[b], J. Casademunt[c], A. Hernández-Machado[c], L. Kramer[d]

[a]*Research Institute for Solid State Physics and Optics of the Hungarian Academy of Sciences, P.O.B. 49, H-1525 Budapest, Hungary*

[b]*Dept. de Física Aplicada, Universitat Politècnica de Catalunya, Campus Nord-Ed. B5, J.Girona Salgado s/n, E-08034 Barcelona, Spain*

[c]*Dept. E.C.M., Fac. de Física, Universitat de Barcelona, Diagonal 647, E-08028 Barcelona, Spain*

[d]*Institute of Physics, University of Bayreuth, D-95440 Bayreuth, Germany*

**Abstract**

Free growth properties of the smectic B liquid crystalline phase into the supercooled nematic have been investigated in quasi-two-dimensional geometry. Different orientation combinations of the two phases have been achieved experimentally and the interfacial patterns have been studied and analysed as a function of undercooling. The angular dependence of the surface tension has been deduced from the shape of the interface in thermal equilibrium. The experimentally determined surface tension anisotropy has been incorporated into computer simulations based on the phase-field model. The simulations have reproduced qualitatively the rich variety of morphologies (extending from the faceted shape to fully developed dendrites) observed in the experiments for a given set of undercoolings in three geometries. Anisotropic heat diffusion on the nematic side, relevant to our experimental system has also been introduced. Both in the experiments and in the simulations we find that the growth is faster in the lower heat diffusion direction. 

*PACS:* 05.45. – a

## 1. Introduction

Interfacial patterns in the process of solidification (see e.g. Refs. [1–4]) under typical experimental conditions possess characteristical length scales of 10–100 μm. On this scale the solid and liquid phases can be treated as continuous media separated by a sharp interface. One has

* Corresponding author.

*E-mail addresses:* katona@power.szfki.kfki.hu (T. Tóth-Katona), ab@power.szfki.kfki.hu (Á. Buka).

0370-1573/00/$ - see front matter 
PII: S0370-1573(00)00055-7

a first-order phase transition with latent heat ($L$) released and conducted away from the interface. We here deal with a thin layer geometry, and in the further discussion we will restrict ourselves to two dimensions. In one-component crystal–melt systems one only has to consider the temperature field. If one neglects the convection, the released heat will be transported by diffusion

$$D\nabla^2 T = \frac{\partial T}{\partial t} \ , \tag{1}$$

where $D$ is the heat diffusion coefficient (assumed to be the same in the two phases), and $T$ is the temperature (variable in space and time).

From the energy conservation across the interface one has that the latent heat released at the interface must be equal to the sum of the heat flows from and to the interface i.e.,

$$\frac{v_n L}{c_p} = D(\partial_n T|_l - \partial_n T|_s) \tag{2}$$

where $\partial_n T|_l$ and $\partial_n T|_s$ are the normal temperature gradients on the liquid and solid sides of the interface, respectively, and $c_p$ is the specific heat.

The melt is undercooled by $\Delta T = T_m - T_\infty$, so the temperature in the liquid phase, far from the interface is given by $T_\infty$, while in the crystal phase the temperature is nearly $T_m$, where $T_m$ is the phase transition temperature.

The location of the interface is determined by an extra boundary condition, which describes the local thermodynamic equilibrium of the front and takes into account the Gibbs–Thomson relation and (linear) kinetic effects:

$$T_i(s,t) = T_m[1 - \tilde{d}_0(\theta)\kappa(x,t)] - \frac{1}{\tilde{\mu}(\theta)} v_n \tag{3}$$

where $T_i(s,t) =$ the temperature of the interface, $s = s(x,y) =$ the equation of the interface, $\kappa(x,t) =$ the curvature of the interface, and

$$\tilde{d}_0(\theta) = \tilde{\sigma}(\theta)/L = [\sigma(\theta) + \sigma''(\theta)]/L \ , \tag{4}$$

is the capillary length ($\sigma(\theta)$ – surface tension, $\theta$ – angle enclosed by the normal of the interface and an arbitrary direction).

According to the Gibbs–Thomson correction of the phase transition temperature, a circular interface (isotropic surface tension) with radius $R$ is in thermal equilibrium with its melt at the temperature $T = T_m(1 - \tilde{d}_0/R)$. In general, when the surface tension is anisotropic, the so called surface stiffness $\tilde{\sigma}(\theta)$ appears in the Gibbs–Thomson relation (see e.g. [5,6]).

The last term in Eq. (3) describes the kinetics of the interface, where: $1/\tilde{\mu}(\theta) > 0$ is the kinetic coefficient, $v_n$ the normal velocity of the interface. In general, the front kinetics is also dependent on orientation, because particles (atoms, molecules) can be attached to the crystal from the melt with different efficiency from different directions.

The anisotropy of the surface tension plays an important role in the selection of the growth morphology of the interface (see e.g. [4]). A great number of experiments were done on traditional solid–liquid systems [7–11], most of which have relatively small anisotropy

$$\varepsilon_\sigma = \frac{\sigma_{max} - \sigma_{min}}{\sigma_{max} + \sigma_{min}} \tag{5}$$

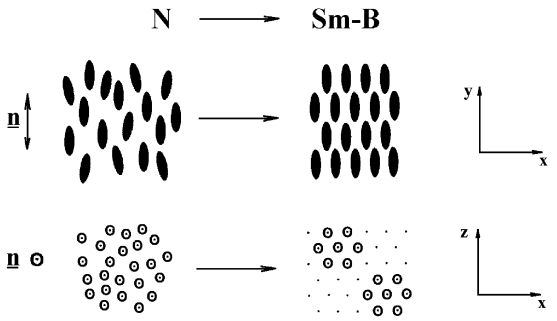


Fig. 1. Schematic illustration of the nematic (N) and smectic-B (Sm-B) phases, and the director **n**.

(only few %) in the surface tension. In contrast, liquid crystalline (LC) systems, as has been shown for the smectic-A (Sm-A)–smectic-B (Sm-B) [12] and for the nematic (N)–Sm-B [13] phase transitions, can have much larger $\varepsilon_\sigma$ with clear facets in the equilibrium shape of the interface. Moreover, in these systems $\varepsilon_\sigma$ can differ by an order of magnitude in different planes of observations with respect to the symmetry axes of the LC phases.

The N–Sm-B phase transition, we studied has a latent heat of typically $L = 4$–$8$ kJ/mol [15], and can be considered as the liquid crystalline analogy of solidification of a pure substance. The N phase is characterized only by the orientational order (described by the director **n**), while the centers of mass of the molecules are distributed randomly as shown in Fig. 1 (see e.g. [14]). The crystalline Sm-B phase (see e.g. [15,16]) has in addition a layered structure (layers are perpendicular to **n**), with a hexagonal packing of the molecules inside the layers. Positional order on large length scales exists both inside and between the layers – see Fig. 1.

Liquid crystals differ from the isotropic melt–crystal systems in the heat diffusion too. The heat diffusion coefficient $D$ is anisotropic both for the nematic (which plays the role of the melt in our observations) and for the smectic phases:

$$D_a = \frac{D_{\parallel} - D_{\perp}}{D_{\perp}} , \tag{6}$$

where $D_{\parallel}$ and $D_{\perp}$ are the diffusion coefficients parallel and perpendicular to **n**, respectively.

Analysing experimental data of $D$ for a number of LC materials, we can assume some general features of the heat transport:

- $D_a > 0$ for nematics. It remains positive also in smectic phases [17], contrary to the mass and electric transport processes, where the anisotropy changes sign at the nematic–smectic transition.
- The magnitude of the average heat diffusion coefficient $D$ and that of $D_a$ in the Sm-B phase do not differ significantly from those in the N phase – see for example [18–20].
- The contribution of the rigid central core of the molecule to the thermal diffusivity is more important than that of the aliphatic end chain [20]. The increase of the alkyl-chain length by one or two carbon atoms does not affect the magnitude of $D$ significantly [18,19].

- $D_a$ depends strongly on the molecular shape. At fixed molecular width, it increases with molecular length. $D_a$ depends primarily on the length of the rigid core [17], but the increase of the alkyl-chain length by one or two carbon atoms increases $D_a$ also [18–20].

## 2. Experimental system

Different liquid crystalline substances were used for observations. Each of them has a first-order phase transition N to Sm-B at $T_{NS}$

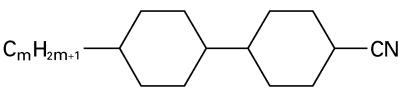


$m = 3$–CCH3, $T_{NS} = 56.3°C$,
$m = 4$–CCH4, $T_{NS} = 53.1°C$,
$m = 5$–CCH5, $T_{NS} = 51.2°C$,

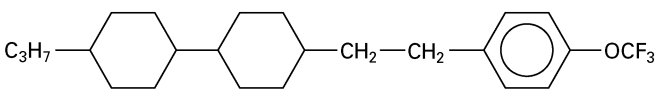


3OCF3, $T_{NS} = 77.0°C$,

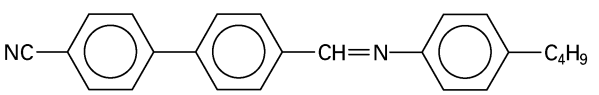


BCBA, $T_{NS} = 87.4°C$.

Samples of both surface alignments of the nematic phase – planar (P, **n** ∥ with the bounding glass plates) and homeotropic (H, **n** ⊥ to the bounding glass plates) – were prepared in cells of dimensions $\approx 20 \times 20\,mm^2$ and of thickness $d = 10\,\mu m$. For planar orientation of the nematic phase we used commercial liquid crystal cells manufactured by E.H.C. Co., Ltd. (Japan). For making cells with homeotropic orientation the glass plates with $SnO_2$ coating have been used. A thin layer of octadecyl-triethoxy-silane, transferred onto the inner surfaces by polymerization, assured the homeotropic alignment.

The sample temperature was controlled in a hot stage with accuracy of 0.002°C. The hot stage was mounted on a polarizing microscope equipped with CCD video camera. The recorded images were fed into a PC for digital analysis, with spatial resolution of $512 \times 512$ and 256 grey scaling for each pixel. With $6.3\times$ objective the scale factors of $1.35 \pm 0.01\,\mu m$/pixel in the $x$ direction and $0.95 \pm 0.01\,\mu m$/pixel in the $y$ direction were determined, so the calculated area of the pixel is $1.28 \pm 0.02\,\mu m^2$.

In the experiments both P and H orientations of the Sm-B phase could be assured, thus different director configurations of the two phases could be investigated. For easier characterization of the system, we introduced symbols. Thus, for example in case of planarly oriented smectic germ in homeotropic nematic surrounding, we used designation P(in H), etc.

## 3. The phase-field model

Numerical treatment of the sharp interface model of solidification as described in the introduction is difficult. It involves either the direct solution of the diffusion equation with the boundary conditions at the moving interface, or the projection of the dynamics onto the interface, which results in a integro-differential equation that is usually solved in the frame of a quasistatic approximation.

In the last years *phase field models* have increasingly been used as an alternative approach to deal with solidification and other free-boundary problems. In these models a nonconserved scalar order parameter or phase field $\phi$ is introduced, whose time evolution equation is coupled with the heat (or impurity) diffusion equation through a source term in order to take into account the boundary conditions at the interface. When the equations are integrated the system is treated as a whole and no distinction is made between the interface and the bulk. The phase field $\phi$ takes distinct values in each of the bulk phases, and it changes continuously between them over a transition layer. The interfacial thickness is then controlled by a dimensionless parameter $\varepsilon$ (see below). This interface width can be related with the actual thickness of the interface of the real system, but in the usual approach it is simply a small parameter that controls the convergence of the model to the sharp-interface equations. The main computational advantage of phase field models is that no boundary condition has to be explicitely applied at the interface.

Phase field models are a variation of *model C* of critical dynamics [21]. The earliest formulations of a phase field model were done by Fix [22] and Langer [23]. A similar model was introduced by Collins and Levine [24], who provided the first link of the phase field model with the sharp-interface model with a kinetic term. Following its introduction, analytical properties of Langer's phase field equations have been studied in detail [25–31]. Penrose and Fife [32,33] provided a framework from which the phase field equations can be derived in a thermodynamically consistent manner from a single entropy functional, rather than from a free energy functional, which made the model applicable to nonisothermal situations. Recently, some additional properties of the solidification front in a supercooled liquid were derived using a phase field model [34].

Early numerical computations of phase field models were performed in one dimension (straight fronts) [35–37], since the method requires quite large computing resources. However, simulations of the model introduced by Kobayashi [38] for dendritic growth of an undercooled melt in two [39] and three [40,41] dimensions showed the capabilities of phase field models for dealing with complex structures. Since then a large amount of simulations have been performed. In the case of solidification problems several phase field models have been developed and tested for realistic situations [42–54]. Some work has also been devoted to the aspect of optimization of the phase field simulations. Specially demanding cases are those with very slow growth, such as the case of small undercooling, or with computationally large systems such as simulations in three dimensions. Karma and Rappel have improved the understanding of the thin interface limit (small but not zero interface width) of the phase field equations [55–57]. This results in a more efficient use of simulations. Moreover, their results allow to deal with arbitrary values of the kinetic coefficient. Further sophistications of the algorithms have also been introduced to improve the quantitative capabilities of the model. These include for instance, the use of rotated lattices, which permit to treat the case of vanishing anisotropy [58], or more recently, the adaptive grid methods [59,60].

In our simulations we used the thermodynamically consistent phase field model derived in Ref. [43]. The explicit expressions for the anisotropies of the surface tension were taken from our experimental results in liquid crystals using the Wulff construction and are given in the following sections. In addition we have included into the model a heat diffusion tensor, which models the anisotropic transport properties of our liquid crystals. The pair of coupled equations for the phase field $\phi(\mathbf{r},t)$ and the dimensionless temperature field

$$u(\mathbf{r},t)=\frac{T-T_{\mathrm{m}}}{\Delta T} \tag{7}$$

are as follows [54]:

$$\varepsilon^2\tau(\theta)\frac{\partial\phi}{\partial t}=\phi(1-\phi)[\phi-\tfrac{1}{2}+30\varepsilon\beta\Delta u\phi(1-\phi)]-\varepsilon^2\frac{\partial}{\partial x}\left(\eta(\theta)\eta'(\theta)\frac{\partial\phi}{\partial y}\right)+\varepsilon^2\frac{\partial}{\partial y}\left(\eta(\theta)\eta'(\theta)\frac{\partial\phi}{\partial x}\right)+\varepsilon^2\nabla(\eta^2(\theta)\nabla\phi)\,, \tag{8}$$

$$\frac{\partial u}{\partial t}+\frac{1}{\Delta}(30\phi^2-60\phi^3+30\phi^4)\frac{\partial\phi}{\partial t}=\nabla_i K_{ij}\nabla_j u\,. \tag{9}$$

The values $\phi=1$ and 0 correspond to the liquid and solid phases, respectively. Lengths are scaled in an arbitrarily chosen length $\omega$, while times are scaled in $\omega^2/D_\perp$. The parameter $\varepsilon=\delta/\omega$ is the dimensionless interface width.

The dimensionless undercooling is

$$\Delta=\frac{c_p\Delta T}{L}\,. \tag{10}$$

The anisotropies of the surface tension and the kinetic term are introduced as [44]

$$\eta(\theta)=\frac{\sigma(\theta)}{\sigma(0)} \tag{11}$$

and

$$\tau(\theta)=\frac{LD_\perp}{\sigma(0)T_{\mathrm{m}}}\frac{\eta(\theta)}{\mu(\theta)}=\frac{c_pD_\perp}{Ld_0}\frac{\eta(\theta)}{\mu(\theta)}\,, \tag{12}$$

where

$$\frac{1}{\mu(\theta)}=\frac{1}{\tilde{\mu}(\theta)}\frac{c_p}{L} \tag{13}$$

and

$$d_0=\frac{\tilde{d}_0\,T_{\mathrm{m}}c_p}{L} \tag{14}$$

The local orientation of the front is given by

$$\tan\theta=(\partial\phi/\partial y)/(\partial\phi/\partial x) \tag{15}$$

The dimensionless parameter $\beta$ is

$$\beta = \frac{\sqrt{2}\omega L^2}{12 c_p \sigma(0) T_m} = \frac{\sqrt{2}\omega}{12 d_0} \ . \tag{16}$$

Finally, the dimensionless heat diffusion tensor is defined by

$$K_{xy} = \frac{D_{xy}}{D_\perp} \ . \tag{17}$$

## 4. Nematic–Smectic-B interface in thermal equilibrium

Slowly heating up the Sm-B and approaching $T_{NS}$ one can achieve a state where only a few Sm-B islands surrounded by the N phase are left and they are separated (usually far) from each other so that no interaction between them is present. Choosing one of these smectic germs for further observation and controlling the temperature (with corrections on the mK scale) in order to keep the size of the germ constant one can approach the thermal equilibrium state of this system. After a few hours of equilibration the shape of the N–Sm-B interface is stabilized. Similar equilibration time ( $\sim 1$ h) has been found in the solvent of organic substance HET [61].

From the shape of the interface in thermal equilibrium we have derived the angle dependence of the normalised surface tension $\eta(\theta)$ by the Wulff construction [62]. This is a geometrical construction based on the fact that the equilibrium shape minimizes the surface free energy – for more details see in the appendix.

### *4.1. Different orientations of the two phases*

The shape of the N–Sm-B interface has been determined in thermal equilibrium with different orientation combinations of the two phases: P(in P), P(in H), H(in H) and H(in P) [63,64].

A faceted, rectangle like, elongated shape (Fig. 2(a) and (b)) has been found for the planar Sm-B. The longer, faceted edges are parallel to the smectic layers (perpendicular to the director) indicating that the Sm-B phase consists of stiff planes (contrary to the Sm-A phase). We point out here that when a facet is present at the melt–crystal interface, it is known (see e.g. [6]) that the advance of the facet can be stuck and might happen that the experimentally determined steady shape of the interface does not reflect the real equilibrium morphology. In such cases a special care should be taken in the process of equilibration, allowing the interface to "breathe".

For the shape anisotropy $(R_{max} - R_{min})/(R_{max} + R_{min})$ ($R$ – distance of the germ perimeter from its nucleation point), which coincides with the surface tension anisotropy $\varepsilon_\sigma$ [65], in P(in P) geometry for CCH3 a value of $\varepsilon_{\sigma 2} = 0.68$ has been measured (number 2 in the subscript denotes the twofold symmetry). In the P(in H) configuration of CCH3 a somewhat smaller value of $\varepsilon$ ($\varepsilon_{\sigma 2} = 0.49$) has been found, due to an additional contribution to the surface energy coming from the elastic deformation of the nematic near the interface which is of splay-bend type along the long edges and mainly twisted along the short ones [63]. On the basis of the experiments, the reproducibility of the ratio $R_{max}/R_{min}$ has been estimated to be below 20% [66]. These values of $\varepsilon_\sigma$ are extremely large compared to that measured in the isotropic melt–crystal systems of other


Fig. 2. The shape of the N–Sm-B interface in thermal equilibrium for CCH3. (a) P(in P), (b) P(in H), (c) H(in H). The director orientations are indicated in both phases.

organic substances (e.g. $\varepsilon_{\sigma 4} = 0.005$ for succinonitrile [9,67], from $\varepsilon_{\sigma 4} = 0.006$ to $\varepsilon_{\sigma 4} = 0.05$ for pivalic acid [9,67–69], $\varepsilon_{\sigma 4} = 0.03$ for camphene [70] or $\varepsilon_{\sigma 6} = 0.003$ for HET [71]). A similarly large value of $\varepsilon_{\sigma 2}$ has been found for the Sm-A–Sm-B interface in buthyloxybenzilidene octylanyline [12], where $\varepsilon_{\sigma 2} \approx 0.5$ has been measured.

With the Wulff construction we determined $\eta(\theta)$ (where $\theta$ describes the interface orientation) by a simple polynomial fit. In case of planar Sm-B for $\theta = 0$ we have chosen the orientation parallel with the smectic layers (perpendicular to the smectic director $\mathbf{n}(S)$). In CCH3 the following functions have been determined [72,52]:

$$\text{for P(in P):} \eta(\theta) = 1.000 - 0.352\theta^2 + 0.008\theta^4$$

$$\text{for P(in H):} \eta(\theta) = 1.037 - 0.0278\theta^2 - 0.022\theta^4,$$

in the range $|\theta| \leq \frac{1}{2}\pi$ (further angle segments can be obtained by continuing $\eta$ symmetrically and periodically). Clearly $\eta(\theta)$ has cusps at $\theta = \pm \frac{1}{2}\pi$ that are associated with the facets.

A totally different equilibrium morphology of the interface has been found in H(in H) configuration, where the shape of the interface was nearly circular with a small hexagonal modulation, reflecting the sixfold symmetry inside the Sm-B layers. The value of $\varepsilon_{\sigma 6} \leq 0.03$ has been measured in this configuration for CCH3 (Fig. 2(c)) [72], and $\varepsilon_{\sigma 6} \leq 0.005$ for CCH5 [64] and these values are essentially equal with the amplitude of the basic Fourier mode $\cos(6\theta)$.

In the H(in P) configuration, which has been studied for CCH5, the additional contribution to surface energy coming from the elastic deformations leads to the superposition of a twofold anisotropy of the surface tension onto the sixfold symmetry of the interface. This results in a slightly oval equilibrium shape. The analysis of the equilibrium shape by Wulff construction gives a value for this twofold anisotropy $\varepsilon_{\sigma 2}$ in the range between 0.01 and 0.03 [64].

### *4.2. Different substances*

A similar equilibrium shape of the interface (faceted long sides and convex short ones) has been found like that in CCH3 (Fig. 2(a)) for substances 3OCF3 and BCBA in the P(in P) configuration, though their molecular structure differ from that of CCH3. Moreover, the shape anisotropies were similar to that in CCH3 (within the scattering described in the Section IV.A.). For 3OCF3 a value of $\varepsilon_{\sigma 2} = 0.66$ has been measured, while in BCBA: $\varepsilon_{\sigma 2} = 0.59$ [66].

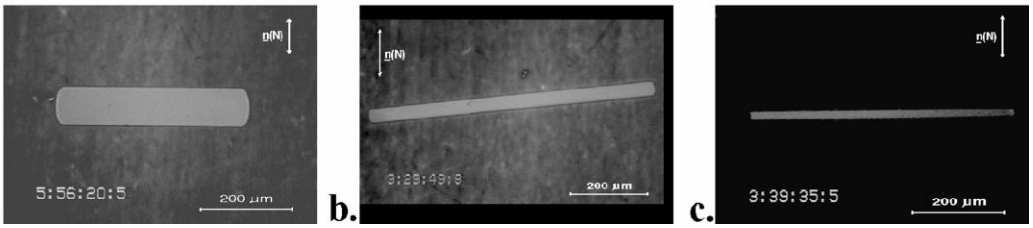


Fig. 3. The shape of the N–Sm-B interface in thermal equilibrium (P(in P) configuration) for: (a) CCH3, (b) CCH4, (c) CCH5. The arrows show the director orientation in the nematic phase.

In contrast, the shape anisotropy of the interface in thermal equilibrium is unexpectedly different for the three homologues of the CCH$m$ ($m = 3, 4, 5$) series. Much larger values of $\varepsilon_{\sigma 2} = 0.89$ and 0.94 have been found for CCH4 and CCH5, respectively, compared to that in CCH3 ($\varepsilon_{\sigma 2} = 0.68$) [53] – see Fig. 3. These considerable differences in $\varepsilon_{\sigma 2}$ for the three homologues have been interpreted by differences in the molecular packing of the Sm-B phase [53]. According to the interpretation (based on the X-ray diffraction investigations [73]), the faceted part of the interface is more rough on the molecular scale in the CCH5 compared to that in CCH4 and in CCH3 especially. Because of this roughness the packing between the N and Sm-B phases is presumably better for CCH5, which leads to a smaller surface tension on the faceted sides, and consequently to higher anisotropy in the surface tension.

The Wulff-construction gave for $\eta(\theta)$ in P(in P) geometry, the following fitting functions (direction corresponding to $\theta = 0$ has been chosen parallel to the smectic layers again):

in CCH3: $\eta(\theta) = 1.000 - 0.352\theta^2 + 0.008\theta^4$ [52],
in CCH4: $\eta(\theta) = 1.000 - 0.445\theta^2 + 0.026\theta^4$ [52],
in CCH5: $\eta(\theta) = 1.00 - 0.47\theta^2 + 0.03\theta^4$ [53],
in the range $|\theta| \leq \frac{1}{2}\pi$.

On the basis of the analysis of the equilibrium shape of the N–Sm-B interface, the connection of the faceted long sides to the convex short ones seems to be continuous, without any cusps in all investigated substances. It means that all surface orientations occur (no "forbidden" directions) and the surface stiffness $\sigma(\theta) + \sigma''(\theta)$ is positive everywhere (see e.g. [74]) (the only exception might be CCH5, where the extremely large anisotropy makes it difficult to analyse the Wulff's plot at the critical regions). In contrast, the Sm-B–Sm-A interface was found to be cusped at the short ends [12]. The question whether this qualitatively different behaviour of the surface tension in the two systems has some fundamental relevance is still open.

## 5. Growth at lower undercoolings

For small undercoolings $\Delta T < 0.2^{\circ}$C no nucleation of the Sm-B phase occurred on time scales of hours. Thus, for such small undercoolings and for precise quantitative measurements we used a previously prepared Sm-B germ during several cooling-heating cycles. The procedure of obtaining the germ was similar to that described in Section 4 for thermal equilibration. In order to assure

similar initial conditions, the size of the germ was fixed (always 400–500 $\mu m^2$) before applying the actual undercooling. The proper experimental procedure (described in [65]) allowed us to get a Sm-B seed with homeotropic orientation besides the planar one.

In the following subsections we describe morphological transitions depending on $\Delta T$. In general, three growth regimes have been found as a function of $\Delta T$, for both P(in P) and H(in H) configuration. These regimes could be distinguished in the morphology and in the growth dynamics. These growth regimes will be presented in the following subsections for the P(in P) and H(in H) configurations, while the H(in P) case is discussed in the Section 7.

We also give a comparison between the experiments and the phase-field model simulations. The phase-field model Eqs. (7) and (8) have been solved numerically on a rectangular lattice. Both equations have been discretized spatially using first-order finite differences on a uniform grid mesh spacing $\Delta x$. An explicit time-differencing scheme has been employed for Eq. (7) and the time step $\Delta t$ has been adjusted in each case in order to avoid numerical instability. Eq. (8) has been solved by the alternating-direction implicit method (ADI), which is unconditionally stable [45]. We have simulated the experimental system by locating the initial Sm-B seed ($\phi = 0$, $u = 0$) either in the lower left corner or in the center of the mesh. In the rest of the system $\phi = 1$, $u = -1$ have been set initially. In absence of experimental data about $(1/\mu(\theta))$, for P(in P) configuration we have taken

$$\tau(\theta) = n\eta(\theta) , \tag{18}$$

where $n = \text{const}$, which implies that the kinetic term remains isotropic (see Eq. (12)).

For simulations in H(in H) configuration, a sixfold anisotropy in the kinetic coefficient

$$\frac{1}{\mu(\theta)} = \frac{1}{\mu_0}(1 + \varepsilon_{\mu 6}\cos(6\theta)) , \tag{19}$$

has been taken into account, with $\varepsilon_{\mu 6} = -0.003$. This value has been obtained by careful adjustment of $\varepsilon_{\sigma 6}$ (in the range of $\varepsilon_{\sigma 6} \leq 0.005$ in accordance to the experiments) and of the $\varepsilon_{\mu 6}$ in numerical simulations until all the experimentally observed growth morphologies at different undercoolings are reproduced [64]. This implies that parameter $\tau(\theta)$ in H(in H) configuration has the form:

$$\tau(\theta) = \tau_0\eta(\theta)[1 + \varepsilon_{\mu 6}\cos(6\theta)] . \tag{20}$$

In all simulations the relevant, experimentally determined functions $\eta(\theta)$ have been used. In the simulations presented in Sections 5 and 6 an isotropic heat diffusion has been taken, while in those discussed in Section 7 the $D_a$ of the nematic phase is taken into account. Other details of the simulation procedure are given elsewhere [52].

### 5.1. Quasi-equilibrium growth regime

In a narrow range of undercoolings, typically $\Delta T \leq 0.06^\circ C$ for planar and $\Delta T < 0.1^\circ C$ for homeotropic Sm-B, a slow growth of the interface has been observed. Its shape has been found not much different from that in thermal equilibrium (the interface is stabilized by the surface tension in this growth regime).

In case of a planar Sm-B the long sides of the interface stay faceted, till the radius of curvature at the short (convex) sides becomes larger than in thermal equilibrium (compare Figs. 4(a) and 2(a))

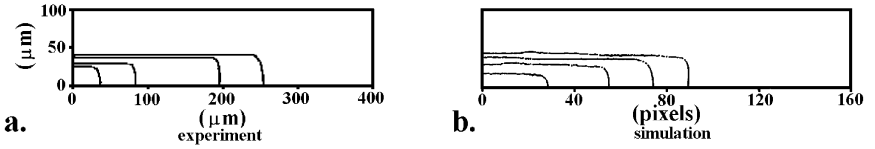


Fig. 4. Qualitative comparison of the experimental and phase-field simulation results for CCH3 in quasi-equilibrium growth regime – P(in P) configuration. The figure shows a quarter of the experimental microscopic images and simulation of the Sm-B–N interface shown by plotting the contours of the patterns taken at subsequent times on top of each other. (a) Experiment, $\Delta T = 0.08^{\circ}\mathrm{C}$, $t = 11.7$; 83.7; 414.7; 608.1 s. (b) Simulation, $300 \times 300$ grid points, $\varepsilon = 0.005$, $\Delta x = 0.005$, $\beta = 350$, $n = 20$, $\Delta t = 10^{-4}$, $\Delta = 0.05$, $t = 0.14$; 0.42; 0.70; 0.98.

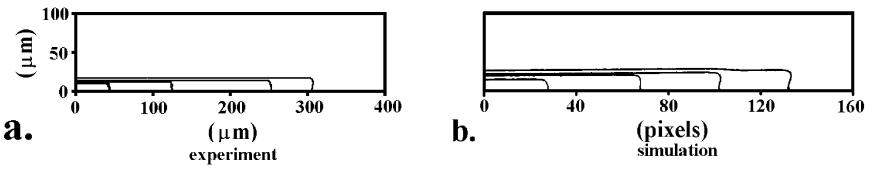


Fig. 5. The same as Fig. 4 for CCH4. (a) Experiment, $\Delta T = 0.04^{\circ}\mathrm{C}$, $t = 20$; 85; 180; 220 s. (b) Simulation, $300 \times 300$ grid points, $\varepsilon = 0.005$, $\Delta x = 0.003$, $\beta = 350$, $n = 20$, $\Delta t = 1.2 \times 10^{-5}$, $\Delta = 0.075$, $t = 0.03$; 0.09; 0.15; 0.21.

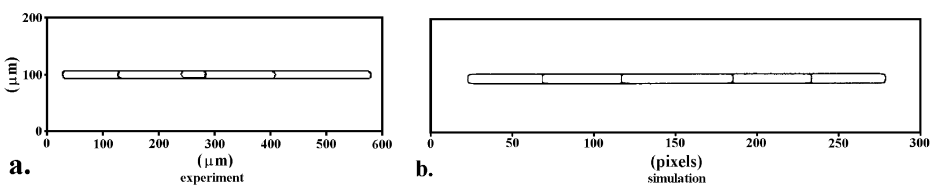


Fig. 6. The same as Fig. 4 for CCH5. (a) Experiment, $\Delta T = 0.08^{\circ}\mathrm{C}$, $t = 20$; 120; 332.7 s. (b) Simulation, $300 \times 300$ grid points, $\varepsilon = 0.005$, $\Delta x = 0.005$, $\beta = 350$, $n = 20$, $\Delta t = 9 \times 10^{-6}$, $\Delta = 0.11$, $t = 0.036$; 0.090; 0.144.

with cusps at the locations where the convex sides connect with the facets. Such properties of the interface growth have been observed in all investigated substances (see Figs. 4, 5 and 6(a)), and confirmed by the computer simulations (Figs. 4(b)–6(b)). The shape anisotropy of the interface increases in time (the growth velocity of the facets is smaller than that of the convex part of the interface) in both experiments and simulations. The increment of the shape anisotropy shows that the expansion of the already existing smectic layers is more favourable than the creation of new ones. The propagation of the facets in CCH5 could be even stopped (see Fig. 6).

In the quasi-equilibrium growth regime the H(in H) pattern at the beginning has a nearly circular shape with a small hexagonal modulation (see Fig. 7(a)) and in the later stage of the growth it becomes irregular – "puddle shaped". The simulation (Fig. 7(b)) qualitatively reproduces the experiment again. Note that in the simulation presented in Fig. 7(b), as well as for all simulations in H(in H) configuration, a sixfold anisotropy in the kinetic coefficient has been taken into account, with $\varepsilon_{\mu 6} = -0.003$ [64].

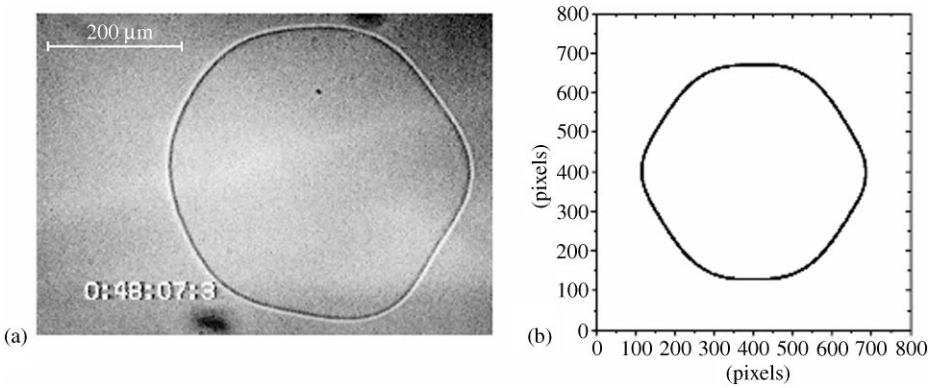


Fig. 7. Qualitative comparison of the experimental and phase-field simulation results for CCH5 in quasi-equilibrium growth regime – H(in H) configuration. (a) Experiment, $\Delta T = 0.05^{\circ}$C. (b) Simulation, $800 \times 800$ grid points, $\varepsilon = 0.005$, $\Delta x = 0.005$, $\beta = 350$, $\Delta t = 10^{-4}$, $t = 8$, $\Delta = 0.1$, $\tau_0 = 20$.

The dynamics of the interface in this quasi-equilibrium growth regime can be understood by diffusive slowing down of a compact interface which leads to the time dependent growth velocity decreasing with $t^{-C}$ where $C = \frac{1}{2}$ – see e.g. [3]. We have measured the spatially averaged growth velocity ($\mathrm{d}\sqrt{A}/\mathrm{d}t$), where $A$ is the area of the Sm-B germ. In CCH3, at the undercoolings of $\Delta T = 0.04^{\circ}$C (P(in P) configuration), $\Delta T = 0.05^{\circ}$C (P(in H)) and $\Delta T = 0.05^{\circ}$C (H (in H)) the values of $C = 0.59$, $C = 0.52$ and $C = 0.56$ have been determined, respectively. For the simulation presented in Fig. 4(b) the value of $C = 0.46$ has been found [66].

### 5.2. Intermediate growth regime

In the next range of undercooling i.e., for the planar Sm-B typically $0.06^{\circ}\mathrm{C} < \Delta T \leq 0.1^{\circ}\mathrm{C}$ and for the homeotropic Sm-B in the range of $0.1^{\circ}\mathrm{C} \leq \Delta T < 0.2^{\circ}\mathrm{C}$, a change in the growth morphology has been observed.

The short sides of the planar Sm-B germ become concave, but the facets still persist parallel to the Sm-B layers (Fig. 8(a)). The destabilization of the interface is observable in this regime: four main branches are formed which grow parallel to the Sm-B layers.

In the H(in H) geometry tips are formed and a petal shaped morphology of the interface appears (Fig. 9(a)) similarly to the experiments on the hexagonal columnar phases [75,76]. The tips reflect the hexagonal symmetry of the Sm-B layers. For $0.1^{\circ}\mathrm{C} < \Delta T < 0.2^{\circ}\mathrm{C}$ the tips split up, but for $\Delta T = 0.2^{\circ}$C six stable dendritic tips are formed in CCH5 (see Fig. 9(c)). More or less expressed dendrites have been observed in the range of undercooling between 0.15 and 0.3°C for CCH5.

For the dynamics of the interface in case of CCH3 we found ($\mathrm{d}\sqrt{A}/\mathrm{d}t$) = const both in P(in P) and H(in H) configurations [72]. The growth rate of the perturbation has also been found constant in time for both configurations [66].

The simulations have reproduced the first destabilization of the interface for both P(in P) – Fig. 8(b), and H(in H) – Fig. 9(b) configurations. Moreover, for larger undercoolings the dendritic growth in the H(in H) case was also observed (Fig. 9(d)).

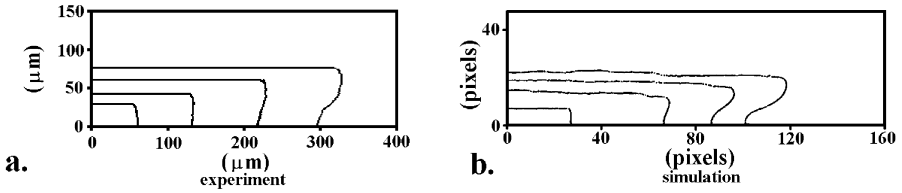


Fig. 8. The same as Fig. 4, for CCH3 in the intermediate growth regime – P(in P) configuration. (a) Experiment, $\Delta T = 0.1^{\circ}$C, $t = 32.8$; 113.0; 253.3 s. (b) Simulation, $300 \times 300$ grid points, $\varepsilon = 0.005$, $\Delta x = 0.005$, $\beta = 350$, $n = 20$, $\Delta t = 10^{-4}$, $\Delta = 0.09$, $t = 0.08$; 0.32; 0.56; 0.80.

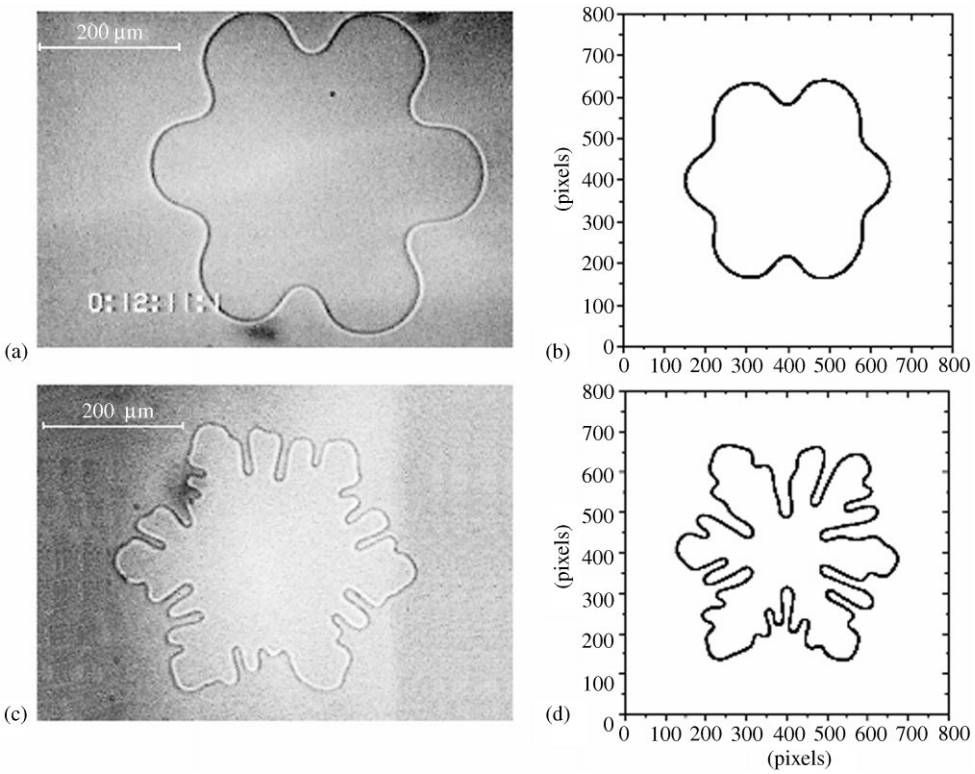


Fig. 9. The same as Fig. 7, for CCH5 in the intermediate growth regime – H(in H) configuration. (a) Experiment, $\Delta T = 0.1^{\circ}$C. (b) Simulation, $800 \times 800$ grid points, $\varepsilon = 0.005$, $\Delta x = 0.005$, $\beta = 350$, $\Delta t = 10^{-4}$, $t = 2.8$, $\Delta = 0.2$, $\tau_0 = 20$. (c) Experiment, $\Delta T = 0.2^{\circ}$C. (d) Simulation, $800 \times 800$ grid points, $\varepsilon = 0.005$, $\Delta x = 0.005$, $\beta = 350$, $\Delta t = 10^{-4}$, $t = 0.42$, $\Delta = 0.5$, $\tau_0 = 20$.

### 5.3. *Fast growth regime*

With further increase of the undercooling, for the planar Sm-B typically $\Delta T > 0.1^{\circ}$C, and for the homeotropic Sm-B typically $\Delta T > 0.2^{\circ}$C, a new growth regime appears.

The morphology of the planar Sm-B changes continuously with $\Delta T$. The facets disappear and the interface roughens up – see Fig. 10(a). The four main branches do not grow parallel to the Sm-B

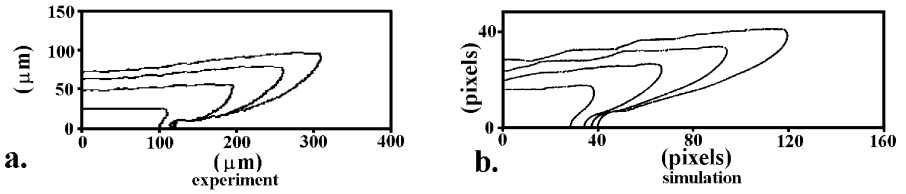


Fig. 10. The same as Fig. 4, for CCH3 in the fast growth regime – P(in P) configuration. (a) Experiment, $\Delta T = 0.12°C$, $t = 8.3$; 17.1; 23.4; 28.1 s. (b) Simulation, $300 \times 300$ grid points, $\varepsilon = 0.005$, $\Delta x = 0.005$, $\beta = 350$, $n = 20$, $\Delta t = 10^{-4}$, $\Delta = 0.2$, $t = 0.06$; 0.12; 0.18; 0.24.

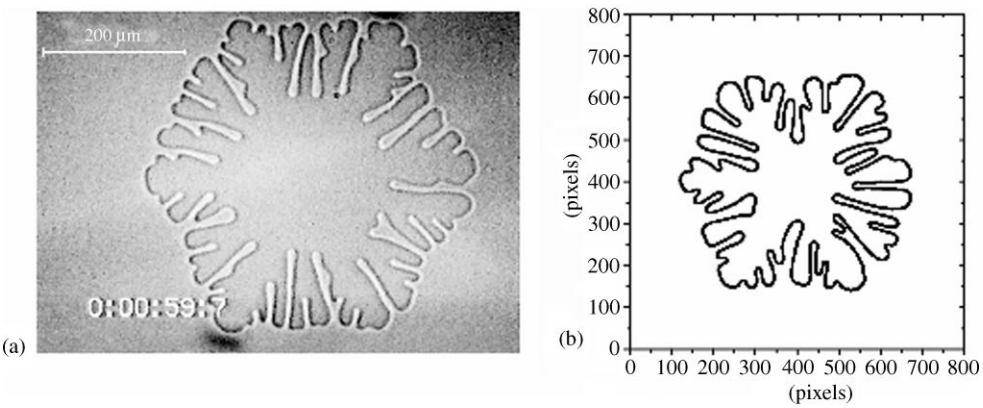


Fig. 11. Same as Fig. 7, for CCH5 in the fast growth regime – H(in H) configuration. (a) Experiment, $\Delta T = 0.35°C$. (b) Simulation, $800 \times 800$ grid points, $\varepsilon = 0.005$, $\Delta x = 0.005$, $\beta = 350$, $\Delta t = 10^{-4}$, $t = 0.25$, $\Delta = 0.6$, $\tau_0 = 20$.

layers (as in Fig. 8), but make an angle with each other which increases in time for $CCH_3$, (the growth direction of the tips changes in time). For $\Delta T \geq 0.5°C$ one gets a dendritic growth with steady growth direction and with four main branches that enclose an angle $\approx 90°$ for CCH3. For such undercoolings the morphology of the interface is not much different from that discussed in Section 6.1.

For the H(in H) configuration in $CCH_5$, the dendritic growth presented in Fig. 9(c) becomes less expressed with increasing undercooling, and finally for large enough $\Delta T$ one gets the dense-branching morphology (see Fig. 11(a)). The enveloping curve of the interface preserves the hexagonal shape having the same orientation of the maxima ($R_{max}$) as in the quasi-equilibrium growth regime (i.e., an analogous angular dependence of the kinetic coefficient should be assumed to that of the surface stiffness which means if $\varepsilon_{\sigma 6} > 0$ one needs $\varepsilon_{\mu 6} < 0$). This is in contrast with the observations made on columnar hexagonal phase [77], where the hexagonal shape of the crystal at low (surface tension controlled regime) and at high (kinetic regime) undercoolings was rotated by $30°$ with respect to each other. On the other hand, the experimentally observed morphological transition: compact interface – petal shape – dendritic growth – dense-branching morphology as a function of $\Delta T$ is in a good agreement with the morphological phase diagrams predicted in [78,79].

The results of the computer simulations clearly show the destabilization of the facets (Fig. 10(b)) for planar Sm-B and the appearance of the dense-branching morphology with a sixfold symmetry for the homeotropic Sm-B (Fig. 11(b)), as observed in the experiments.

For both, planar and homeotropic Sm-B of CCH3, $(\mathrm{d}\sqrt{A}/\mathrm{d}t)$ asymptotically tends to a constant value determined by $\Delta T$ [72], which is in agreement with the generic feature of growth phenomena after the equilibrium morphology has become unstable [79,80].

Finally, one should mention that comparison of the numerical calculations with the experimental results can be made only on the qualitative level due to the limitations of the phase field model described in [55]. However, the model turned out to be quite sensitive to the anisotropies $\varepsilon_\sigma$ and $\varepsilon_\mu$. For example the change of one of the anisotropies in H(in H) geometry by a factor of 2 results in a pronounced modification of the growth shape, or even induces a morphological phase transition for some undercoolings [81].

## 6. Nucleation and growth at higher undercoolings

The growth of the Sm-B phase in the undercooled N initiates with nucleation (on some impurities, orientational defects of the director or defects on the bounding glass plates). For small undercoolings ($\Delta T < 0.2^\circ$C) no heterogeneous nucleation occurred on the time scale of hours. For large enough $\Delta T$, the fast dendritic growth of the Sm-B phase has been observed, always with planar director, independently from the orientation (planar or homeotropic) of the N environment and typically with four main dendritic branches. The growth velocity $v$ of the dendritic tips has been found constant in time and of course undercooling dependent. The only exception is the BCBA for which $v(t) \neq$ const and which is described in [13].

Contrary to the previous section, where the morphological transition depending on $\Delta T$ has been described, in this section we compare different substances (first of all for the CCH$m$ homologues) at the same undercooling $\Delta T = 1.0^\circ$C in P(in P) configuration.

For quantitative characterization of the growing smectic structure the following labels were used (see Fig. 12): $\alpha$ is the angle between the two closer main branches of the dendrite, which coincides

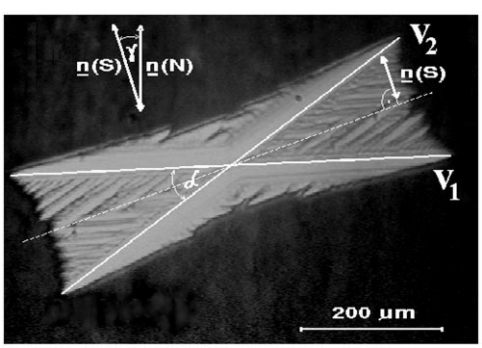


Fig. 12. Notations used for the characterization of the Sm-B growth morphologies: $\underline{n}$(S) and $\underline{n}$(N) – is the director of the Sm-B and N phase, respectively; $\gamma$ the angle between the directors of the two phases; $\alpha$ the (smaller) angle between the two dendritic main branches; $\mathbf{v}_1$ and $\mathbf{v}_2$ the growth velocities of the dendritic tips.

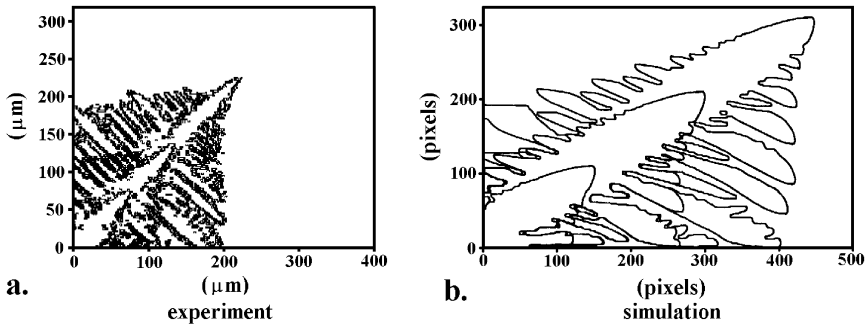


Fig. 13. Qualitative comparison of the experimental and phase-field simulation results for CCH3. (a) Experiment, $\Delta = 1.0°C$, $t = 0.2$; 0.4; 0.6 s. (b) Simulation, $500 \times 500$ grid points, $\varepsilon = 0.003$, $\Delta x = 0.005$, $\beta = 450$, $n = 14$, $\Delta t = 9 \times 10^{-6}$, $\Delta = 0.7$, $t = 0.033$; 0.066; 0.099.

with the angle between a main branch and its side branches; $\gamma$ is the angle between the directors $\mathbf{n}$(N) and $\mathbf{n}$(S); $\mathbf{v}_1$ and $\mathbf{v}_2$ the growth velocities of the dendritic tips.

### 6.1. Dendritic growth in CCH3

In the case of CCH3 we got dendritic growth with four-fold symmetry and parabolic tips. $\alpha \approx 90°$ was found for all germs observed. Strong and symmetric side branching activity, even of second and third generation (see Fig. 13(a)) was observed. The director of the nucleated Sm-B was parallel to the director of the surrounding nematic ($\gamma \approx 0$). In 93% of the 270 germs considered, $\gamma$ was found below 5° and in the remaining 7% it was between 5° and 9°.

In the simulation based on the phase field model (Fig. 13(b)) a fast moving dendrite grew forming a well-defined angle $\alpha$ between the main branches. Side branches appeared on both sides of the main branch enclosing also angle $\alpha$ with it. Some tertiary side arm activity could be observed similarly to experiments, but to reproduce that a large amount of computational time was required. The main discrepancy between the experiments and simulations is that in the latter the angle $\alpha$ has been found noticeably smaller than 90°. In order to improve the situation we should first of all incorporate the anisotropy of the kinetic term on a proper way, because computer simulations [52] showed that the angle $\alpha$ is very sensitive to the angular dependence of the kinetic coefficient.

### 6.2. Dendritic-like growth in CCH4

For CCH4 we get dendritic-like growth, which means that the four main branches are still observable with intensive side branching, but the tips and the length of the side branches are not symmetric with respect to the direction of the normal growth velocity of the tip (see Fig. 14(a)). The angle between the main branches is in the range of $0° \leq \alpha \leq 60°$ and varies from germ to germ, but it does not seem to depend on the undercooling. The angle between the first generation of side branches and the main branch is always $\alpha$. The angle between the nematic and smectic directors ($\gamma$) covers also a wide range: $0° \leq \gamma \leq 80°$. The distribution of $\gamma$ obtained for 270 germs has been presented in [53]. A large part ( $\sim 37\%$) of the germs is still oriented parallel to the $\mathbf{n}$(N), $\gamma = 0$, but

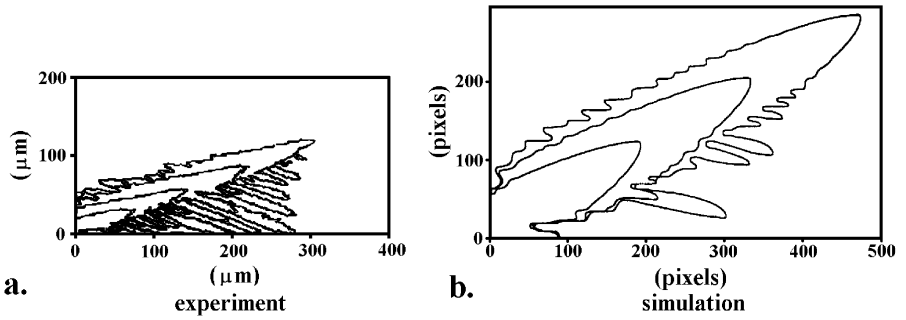


Fig. 14. Qualitative comparison of the experimental and phase field simulation results for CCH4. (a) Experiment, $\Delta = 1.0°C$, $t = 0.5$; 0.9; 1.3; 1.8 s. (b) Simulation, $500 \times 500$ grid points, $\varepsilon = \Delta x = 0.005$, $\beta = 350$, $n = 20$, $\Delta t = 5 \times 10^{-6}$, $\Delta = 0.5$, $t = 0.104$; 0.182; 0.260.

the rest is "disaligned" with respect to the nematic director, thus $\gamma$ reaches values up to 80°. No germs were found with extremely large disalignment in the range of $80° < \gamma < 90°$.

No correlation between $\alpha$, $\gamma$ and $v$ was found, moreover $\alpha$ and $\gamma$ did not show any dependence on the undercooling $\Delta T$. In general, the properties of each germ ($\alpha$, $\gamma$ and $v$) are reproducible in successive experiments provided the sample does not crystallize. But these properties can change at the same location if the sample gets into the crystalline phase and is heated up again.

The morphology obtained by simulations (Fig. 14(b)) corresponds to the one observed experimentally. Again there is a single angle $\alpha$ that characterizes the direction of the main branches, and the same angle can be measured between the main and the first generation of the side branches. The asymmetric side branching with respect to the direction of the normal growth velocity of the main tip has also been reproduced.

### 6.3. *Needle-like growth in CCH5*

For CCH5 the growing Sm-B germ has a faceted shape at any undercooling reminding its equilibrium shape, differing only at the short sides which become unstable (see Fig. 15(a)). Such a morphology can be considered as a limit $\alpha = 0°$. The directors of the N and Sm-B phases show even weaker correlation than for CCH4. Though the distribution of $\gamma$ is in the same angular range for different nucleation centers ($0° \leq \gamma \leq 80°$) as in CCH4, but germs with larger $\gamma$ nucleate more often in CCH5 than in CCH4 i.e., the distribution of the $N(\gamma)$ ($N$ is the number of the Sm-B germs) is smoother. The $\gamma$ and $v$ of the nucleated Sm-B germ at the same location in the sample might change after crystallization in the same way as it was described above for CCH4.

The growth morphology in CCH5 has been computationally reproduced using the parameters indicated in the caption of Fig. 15(b). Faceted edges and unstable short sides are present in the growth shape as it was found in the experiments.

The large variety in the growth morphologies of the N–Sm-B interface observed experimentally and confirmed by computer simulations in CCH*m* homologous series has been explained by the large difference in the surface tension anisotropy [53]. Presumably for CCH5 the surface tension anisotropy is so large (and the cusp in the angular dependence of the surface tension is so deep), that it does not allow the destabilization of the faceted sides (it would involve the appearance of the

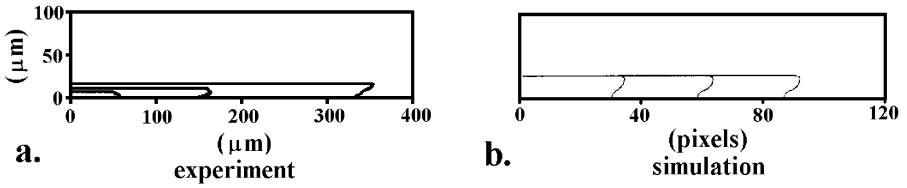


Fig. 15. Qualitative comparison of the experimental and phase-field simulation results for CCH5. (a) Experiment, $\Delta = 1.0°C$, $t = 0.4$; 0.9; 1.3 s. (b) Simulation, $300 \times 300$ grid points, $\varepsilon = \Delta x = 0.005$, $\beta = 350$, $n = 20$, $\Delta t = 8 \times 10^{-6}$, $\Delta = 0.16$, $t = 0.035$; 0.070; 0.105.

orientations that are energetically unfavoured). Only the short rough sides are destabilized as it was seen in experiments (Fig. 15(a)) and also in simulations (Fig. 15(b)), contrary to the CCH4 and especially to the CCH3, where the values of $\varepsilon_{\sigma 2}$ are smaller. This idea is supported by the experiments on the 3OCF3 and BCBA which have similar $\varepsilon_{\sigma 2}$ to that of CCH3 (see in Section 4.2). In 3OCF3 $\alpha \approx 80°$ has been measured [66], while in BCBA $\alpha \approx 90°$ [13] with intensive side-branching activity for both substances.

The asymmetry of the side-branching activity with respect to the growth direction of the main tip in case of CCH4 (see Fig. 14), which has been observed both experimentally and by computer simulation, could be understood by taking into account the angle between the Sm-B director and the normal to the interface. In the vicinity of the tip on that part of the interface where its normal encloses a smaller angle with the smectic director (external side – see Fig. 12) the interface is more stable against the perturbations than on the other (internal) side. This is due to the fact that the coincidence of the surface normal and the director corresponds to the minimum in the angular dependent surface tension. Thus, at this part of the interface the roughening is less expressed (any perturbation involves significant increase of the surface free energy because of large $\varepsilon_{\sigma 2}$), compared to other parts where the angle between the surface normal and the director is larger. This is also noticeable in Figs. 12 and 14. where on the external side of the dendritic tip the side branches became easily faceted, with facets parallel to the smectic layers. These phenomena are in accordance with the observation that in the process of the smectification the expansion of the already existing smectic layers is preferred instead of the creation of new ones.

## 7. Effect of the anisotropy of the nematic phase on the growth patterns

The anisotropy of the nematic phase gives rise to new (relatively weak) effects, that superimpose on the (usually stronger) effects coming from the anisotropy of the smectic phase:

(i) The most interesting phenomena arise due to the anisotropic heat diffusion in the nematic phase. It usually alters the shape of the growing smectic domain if the nematic director is planar.

(ii) We have already shown (Fig. 2(b)) that if the director of the nematic and smectic phases do not coincide, a thin reorientation zone builds up in the nematic phase near the interface. The corresponding elastic deformation usually gives an anisotropic contribution to the surface energy, which depends on the actual configuration and the (anisotropic) elastic properties of the nematic phase.

(iii) The nematic phase may also modify the phase transformation kinetics. Unfortunately, no experimental information is available for this effect.

To analyse the effects coming from the anisotropy of the nematic phase the H(in P) and P(in P) configurations have been taken.

The advantage of the P(in P) configuration is that in this case effect (ii) is absent and the heat diffusion anisotropy dominates (effect (i)). However, one should note that in this configuration the anisotropy in surface tension coming from the structure of the smectic phase is large.

The advantage of the H(in P) configuration is, that the anisotropy of the surface tension is small in the plane of the smectic layers. Thus in this configuration the effects deriving from the smectic anisotropy do not suppress the effects due to the anisotropy of the nematic phase as much as in the P(in P) case. One must add however, that in this configuration all three of the above mentioned effects are present making the analysis difficult.

Let us start with the analysis of the effects caused by the heat diffusion anisotropy. It has been shown in [64,82] that by properly rescaling the coordinate system, and transforming a system with anisotropic heat diffusion into a system with isotropic diffusion, not only the heat diffusion equation (1) will be transformed back to the case of an isotropic system, but also the balance of heat (2). In this representation the heat diffusion anisotropy enters only the Gibbs–Thomson relation as an additional (angular dependent) modulation of the surface stiffness and the kinetic term. In this way, it can be shown that a system with initially isotropic surface tension and kinetic term will develop growing crystals elongated in the direction of the lower heat diffusion (when scaled back to the original coordinate system). This interesting result has also been demonstrated in numerical simulations [54,64].

In the case of CCH4 in the P(in P) geometry the growth shapes reflect strikingly the effect of the anisotropic heat diffusion. Here, as was mentioned in the previous section, a large variety of growth morphologies could be experimentally observed in the range of angles $0 \leq \gamma \leq 80^\circ$ and $0 \leq \alpha \leq 60^\circ$ (see Fig. 12. for notations). In these cases, when $\gamma \neq 0$ and $90^\circ$, a nonreflection symmetry appeared in the growth shape (except the case of $\alpha = 0$). Thus the pair of main branches which have a larger angle with the $\mathbf{n}(N)$, have larger growth velocity $|v_1|$ than the other pair ($|v_2|$) – see Fig. 12 for notations. Therefore the tip's growth is preferred in the direction of the lowest heat diffusion (direction $\perp$ to $\mathbf{n}(N)$).

The observed relative difference in the growth velocities $\delta v = (|v_1| - |v_2|)/|v_1|$ reached the value 0.2 in some cases. A nonmonotonous angular dependence $\delta v(\gamma)$ has been experimentally observed and reported in [54] with a maximum around $\gamma = 45^\circ$. Taking into consideration the uniaxial nature of the nematic phase, a behaviour is expected with $\delta v = 0$ for $\gamma = 0$ and $90^\circ$ as seen in the experiments.

In order to reproduce the growth morphologies observed in CCH4 for $\gamma \neq 0$ (see Fig. 16(a)), the experimentally determined $\eta(\theta)$ function has been rotated in the simulation by $\gamma$ in the $(x, y)$-plane and the anisotropy in the heat diffusion coefficient has been added. On the basis of the heat diffusion anisotropy measurements [17–19] we estimated $D_a$ in CCH$m$ ($m = 3, 4, 5$) homologues [53]. The estimated value of $D_a$ has been included into simulations based on phase field model – see Eqs. (9), (12) and (17). Preliminary measurements [83] carried out very recently on CCH5 show that the value of $D_a$ is even larger from that estimated in [53].

As Fig. 16(b) shows, the reflection symmetry has been broken by including the anisotropic heat diffusion only (previous simulations with rotated surface tension function and isotropic $D$ did not show the asymmetry in the growth velocities).

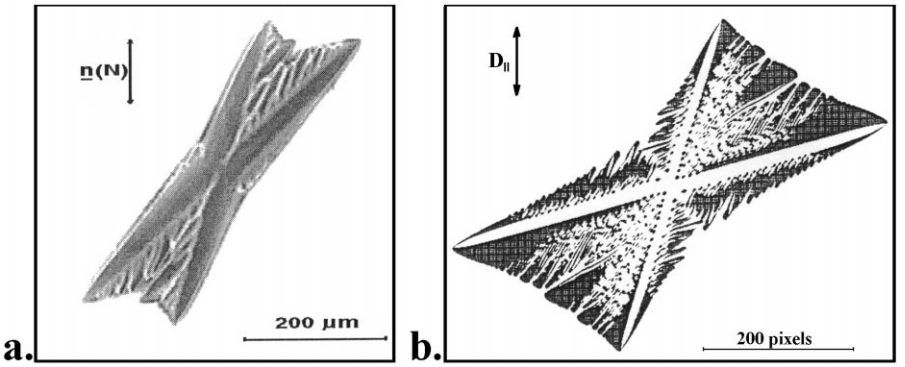


Fig. 16. Qualitative comparison of the experimental and phase field simulation results for CCH4 with the influence of the anisotropic heat diffusion coefficient which causes a growth with nonreflection symmetry in P(in P) configuration. (a) Experiment, $\Delta T = 1.0^{\circ}$C, $\gamma = 58^{\circ}$. (b) Simulation, $600 \times 600$ grid points, $\varepsilon = 0.005$, $\Delta x = 0.005$, $\beta = 850$, $\Delta = 0.5$, $n = 20$, $\Delta t = 2 \times 10^{-6}$, $t = 0.06$, $D_a = 0.5$.

Remaining in the P(in P) geometry in the experiments with CCH3 and CCH5 the influence of $D_a \neq 0$ on the pattern formation could not be detected directly. As we reported in [53] for CCH3 the germs nucleate with $\gamma \approx 0$, which means that the four main branches grow symmetrically with respect to the fastest heat diffusion direction determined by $\mathbf{n}(N)$. For CCH5 despite of $\gamma \neq 0$ the observed $\alpha = 0$ makes difficult the direct detection of the influence of $D_a$ on the pattern formation.

The influence of the anisotropy of the nematic phase in H(in P) configuration is a combination of three effects observed for the substance CCH5 (see Fig. 17(a)) and analysed in numerical simulations [64]:

(i) The heat diffusion anisotropy also induces an elongation of the germ and the formation of dendritic tips perpendicular to $\mathbf{n}(N)$ [64]. The experimentally observed shape presented on Fig. 17(a) has been compared with numerical simulation including the anisotropy of $D$ only ($D_a = 0.2$) – see Fig. 17(b).

(ii) In this configuration, where a homeotropic Sm-B seed is surrounded by a planar $N$ phase, an additional elastic energy is accumulated at the interface between the two phases which involves a deformation zone in the nematic where the planar $\mathbf{n}(N)$ changes continuously to the homeotropic $\mathbf{n}(S)$. This additional contribution is similar to that mentioned in Section 4.1 for the P(in H) configuration, and involves a twofold anisotropy of the surface tension that superposes onto the sixfold symmetry of the interface given by the hexagonal lattice inside the Sm-B layers. The surface tension function now has the form

$$\sigma(\theta) = \sigma_0(1 + \varepsilon_{\sigma 2} \cos(2\theta) + \varepsilon_{\sigma 6} \cos(6\theta)), \tag{21}$$

where $\varepsilon_{\sigma 6}$ corresponds to the anisotropy determined for H(in H) configuration and described in Section 4.1. The analysis of the equilibrium shape by Wulff construction gave for the anisotropy $\varepsilon_{\sigma 2}$ a value in the range between $-0.01$ and $-0.03$ [64]. It has been shown that the twofold anisotropy $\varepsilon_{\sigma 2}$ causes elongation of the growing Sm-B germ in the direction parallel to $\mathbf{n}(N)$ at undercoolings investigated in [64]. Since the experimentally observed shapes of the interface show elongation perpendicular to $\mathbf{n}(N)$ (see Fig. 17(a)), obviously a different mechanism is responsible for the effect.

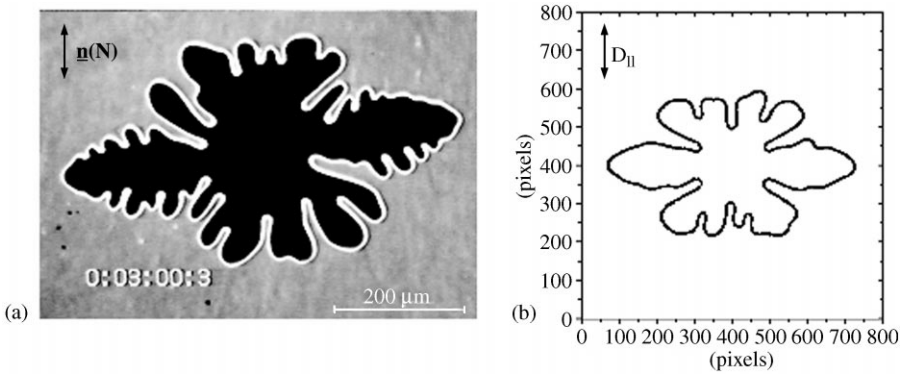


Fig. 17. Qualitative comparison of the experimental and phase field simulation results for CCH5 in – H(in P) configuration. (a) Experiment, $\Delta T = 0.15°C$. (b) Simulation, $800 \times 800$ grid points, $\varepsilon = 0.005$, $\Delta x = 0.005$, $\beta = 350$, $\Delta t = 10^{-4}$, $t = 0.36$, $\Delta = 0.5$, $\tau = 20$, $D_a = 0.2$.

(iii) In H(in P) configuration the attachment kinetics of the molecules is supposed to depend on the angle enclosed by the surface normal and $\mathbf{n}(N)$. On the part of the interface, where the surface normal is perpendicular to $\mathbf{n}(N)$, the reorientation of the director from planar to homeotropic involves twist deformation and the kinetics should be faster than on the other parts of the interface, where the reorientation involves splay deformation mainly. This appears indeed plausible because the evolution of a twist distortion involves no backflow, in contrast to the evolution of splay [84]. Alternatively, on the molecular level, one might argue, that on the part of the interface, where the surface normal is perpendicular to $\mathbf{n}(N)$ the molecules should only rotate in order to achieve the H orientation. On the other part of the interface, where the surface normal is parallel with $\mathbf{n}(N)$, in addition to the rotation the mass centre of the molecules should be translated, since the length of the molecules is more than 3 times larger than their diameter [73]. This effect can be described by including a twofold anisotropy $\varepsilon_{\mu 2}$ in Eq. (19), similarly to that in the surface tension (Eq. (21)) and will induce an elongation of the growth shape perpendicular to $\mathbf{n}(N)$ as it has been shown in [64].

## 8. Dendrites regularized by spatially homogeneous time-periodic forcing

The side branching structure of dendritic growth (presented in Fig. 12 for example), roughly defines the microstructure of the emerging solid phase and implicitly influences its mechanical, thermal, chemical, and other properties. Therefore, the control of the dendritic side branching besides of academic aspects has practical importance too in designing materials.

A spatially inhomogeneous controlling of dendritic side-branching has already been achieved by periodic local heating of the dendrite tip by laser beam [89–91], or by oscillatory flow field [92]. On the other hand, in many respects it is more suitable to control the side branching by non-local, spatially homogeneous time-periodic forcing. In [93] we propose two methods by pressure oscillations and by uniform periodic heating in the volume. Periodic pressure modulations induce oscillations of the phase transition temperature homogeneously and instantaneously in

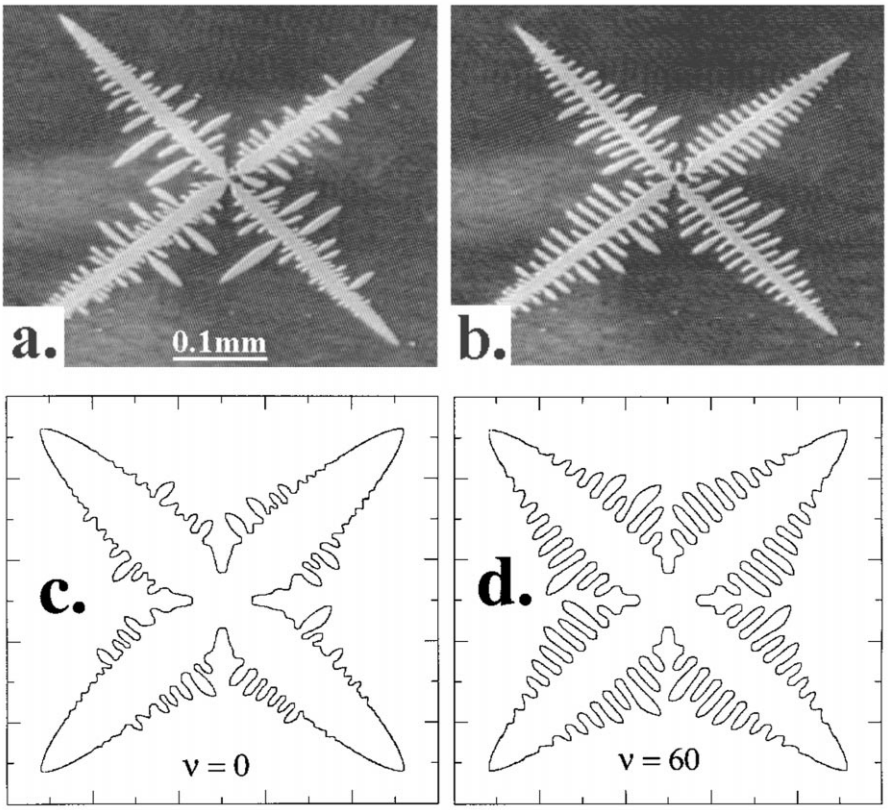


Fig. 18. Effect of pressure oscillations on the Sm-B dendrite growing in undercooled N phase. (a) Experiment, no pressure oscillations, $\Delta T = 1.0°C$. (b) Experiment, $\Delta T = 1.0°C$, $p_e = 2$ bar, $\xi = 0.2$. (c) Simulation, no pressure oscillations, $\Delta = 0.55$, $1000 \times 1000$ grid points, $\varepsilon = 0.005$, $\Delta x = 0.005$, $\beta = 350$, $\Delta t = 10^{-4}$, $t = 0.24$, $\tau = 20$, $\varepsilon_{\sigma 4} = 0.06$, $\varepsilon_{\mu 4} = 0.12$. (d) Simulation, pressure oscillations with frequency $\nu = 60$, amplitude $a_0 = 0.2$ and $\xi = 0.3$. Other parameters as in (c).

large volumes according to the Clausius–Clapeyron relationship, while periodic heating of the sample induces an oscillation in the temperature of the undercooled melt.

In the experiments CCH3 has been used in P(in P) geometry. The setup described in Section 2 has been slightly modified. For pressure modulation the liquid crystal cell was placed into a hermetically closed brass box surrounded by the hot stage. The gas pressure in the brass box has been regulated by a computer controlled valve system that switches off and on the excess pressure $p_e$ preset between 0 and 2 bar. The modulated heat release in the bulk has been realized by periodically transmitting an AC electric current through the LC layer. Square-wave oscillations of both pressure and electric current have been applied with filling coefficient $\xi = t_{on}/t_0$, where $t_0$ is the period of the oscillations and $t_{on}$ stands for the pulse length. Measurements have shown that under well defined conditions both types of oscillatory perturbations can be used to control the side-branching process. This is illustrated in Fig. 18(a) and (b) for undercooling $\Delta T = 1.0°C$. Fig. 18(a) shows a snapshot of the growing Sm-B dendrite without imposed oscillations, while the

regular resonance pattern in Fig. 18(b) has been achieved by pressure oscillations $p_e = 2$ bar with $\xi = 0.2$. Similar resonance patterns to that in Fig. 18(b) appeared when electric current oscillations have been applied with a period averaged heating power of about $0.6 \times 10^{-4}$W/cm$^2$ at $\Delta T = 1.0°$C. Pressure oscillations of $p_e = 2$ bar modulate the phase transition temperature by about 0.07°C (the pressure coefficient of the phase transition temperature has been found about 0.035°C/bar), while a period averaged heating power of $0.6 \times 10^{-4}$ W/cm$^2$ causes temperature variations of 0.1–0.2°C in the melt (that is an overestimate).

The experimentally observed resonance patterns have been reproduced by phase field equations (8) and (9) with modifications described in [93]. Here, we summarize the essence of these modifications only. To avoid difficulties when introducing an oscillatory melting point, $u$ is related to a reference temperature $T_r$ instead of the melting point $T_m$. For pressure modulations a time-dependent term $A(t) = a_0 f(t)$ has been incorporated into Eq. (8), while periodic heating was represented by a source term $B(t) = b_0 f(t)$ in the heat transport equation (9).

Numerical calculations without perturbations ($A(t) = 0$ and $B(t) = 0$) result in dendritic growth with essentially random side-branching [Fig. 18(c)] similarly to the experiments [Fig. 18(a)]. Pressure oscillations ($A(t) \neq 0$) or heating modulations ($B(t) \neq 0$) produce regular resonance patterns [see e.g. Fig. 18(d)] as seen in the experiments [Fig. 18(b)]. The formation of the side branches and the tip velocity show a strict correlation with pressure (undercooling) pulses both in simulations and in experiments.

Finally, one can investigate the parameter space that defines the range of conditions under which pressure (or undercooling) oscillations dominate the pattern formation. This parameter space consists of the amplitude and the frequency of oscillations, the undercooling, and the anisotropy (both in the surface tension and in the kinetic term). Results of these investigations can be summarized as follows. The increase of the amplitude $a_0$ (or $b_0$) of the oscillations naturally enhances the response of the system – more regular patterns appear. Oscillation dominated patterns [as in Figs. 18(b) and (d)] have been observed in a broad range of modulation frequencies [93], but as the frequency increases further, the uncorrelated thermal side branching similar to those in Figs. 18(a) and (c) reappears. Increasing the undercooling the tendency for spontaneous side branching becomes more pronounced and the external perturbations need only to regulate them. Consequently, with increase of $\Delta$, smaller amplitudes are sufficient to obtain oscillation driven side branching. Numerical calculations have also shown that decreasing the anisotropy of the system, the regularity of the patterns also decreases.

## 9. Concluding remarks

We have presented an extended experimental investigation of the N–Sm-B interface in thermal equilibrium as well as that of the non-equilibrium growth of the free interface. The experimental results were reproduced qualitatively by computer simulations based on the phase field model using the experimentally determined function $\eta(\theta)$.

The fact that in thermal equilibrium the hexagonal order within the Sm-B layers does not lead to faceting of the interface in the H(in H) configuration (see Fig. 2(c)) is consistent with general principles excluding faceting in two-dimensional crystals with short-range interaction, see e.g., [85,86]. This is presumably applicable here because the correlation of the hexagonal ordering

between layers is weak. By contrast, the faceting along the Sm-B layers in P(in P) configuration (see Figs. 2(a), (b) and 3) is not excluded because the extension of the facets is much larger than the molecular dimensions.

A sequence of morphological transitions: compact interface with facets (Figs. 4(a)–6(a) and 8(a)) – "butterfly" morphology (Fig. 10(a)) – dendrites (Figs. 12–14(a)) has been observed in the P(in P) and P(in H) configurations as a function of $\Delta T$. In H(in H) configuration the observed morphological transition sequence was: compact interface (Fig. 7(a)) – petal shape (Fig. 9(a)) – dendrites (Fig. 9(c)) – dense-branching morphology (Fig. 11(a)).

All the basic growth morphologies have been reproduced by computer simulations based on phase field model. Although the set of parameters used in the computer simulations might differ from the real material constants (except the $\eta(\theta)$), the qualitative resemblance is remarkably good. This resemblance shows that the phase field model is able to handle strongly anisotropic interfaces with facets in a rather simple way. Furthermore, the results show that the surface tension anisotropy is the most dominant factor in determining the morphologies in the complex growth processes observed in the experiments. Note that computer simulations involving only the surface tension anisotropy (with isotropic heat diffusion and kinetic coefficient) have reproduced completely the qualitative picture of the experimental situation for all investigated substances. This qualitative agreement between experiments and simulations is not complete for CCH3 (which has the lowest surface tension anisotropy among all the investigated substances) at large undercoolings only (see Fig. 13). However, details of the interface shapes at larger undercoolings depend on the kinetic term. As it was mentioned in Section 6, computer simulations [52] showed that the morphology reacts sensitively to the angular dependence of the $1/\mu(\theta)$ at larger $\Delta T$. A direct measurement of the kinetic coefficient would be desirable, but it would involve measuring the growth velocity at much larger undercooling than was reachable experimentally. Measurements based on the interference techniques [94] are in the progress. The kinetic coefficient, including its anisotropy, has been measured for mass transport controlled growth of a hexagonal columnar mesophase [77]. Another concern about the way kinetic effects are incorporated in the model relates to the fact that, when facets are present, the dependence of the kinetic term in Eq. (3) may not be strictly linear in the normal velocity. Other forms have been discussed in the literature, see, e.g. [5,87,88]. In contrast to the anisotropy of the kinetic effects, a nonlinear dependence on the velocity cannot be handled by the phase field model in its present form, and more drastic modifications should be introduced to properly incorporate such effects. However, in view of the qualitative agreement with the experiments, these effects do not seem to affect the basic features. On the other hand the inherent anisotropy of the transport coefficients of liquid crystals have in certain situations affected the growth morphologies. Namely the breaking of the reflection symmetry occurring in shapes grown on CCH4 germs in P(in P) configuration, and the dendrites appearing in H(in P) configuration of CCH5, have been explained in terms of the anisotropy of the heat diffusion coefficient.

## Acknowledgements

T.T.-K. is indebted to the hospitality of the University of Barcelona and Politechnical University of Catalunya. Investigated substances were kindly made avaliable for us by Merck, Darmstadt. The

work was financially supported by EU TMR Project No. ERB FMRX-CT 96-0085 and by research grants No. OTKA T031808 and OTKA F022771. R.G.C., L.R.P., J.C. and A.H.M. thank the Dirección General de Enseñanza Superior (Spain) (Projects PB96-0241-C02-02, PB96-1001-C02-02 and PBR96-0378-C02-01) for support. We also acknowledge the Centre de Supercomputació de Catalunya (CESCA) for computing support.

## Appendix

### *A.1. From the equilibrium shape to the angular dependence of the surface tension – the Wulff construction*

The shape of the crystal in thermodynamic equilibrium with its melt is determined by the free energy per unit area, needed for the formation of the interface. Based on this fact Wulff [62] gave a geometrical construction that relates the surface free energy (or surface tension) $\sigma(\theta)$ and the equilibrium shape of the crystal. According to this construction, the distance measured from the center to the boundary of the crystal is proportional to the surface free energy per unit area in a given direction.

Let us consider an arbitrary equilibrium shape of the interface restricting ourselves to two dimensions (2D). In 2D the phase boundary (Cr) of the crystal is described by the vector $\mathbf{r}(\varphi)$ originating from O. The d$s$ element of the phase boundary at the point A has a normal unit vector $\mathbf{u}$ that encloses an angle $\theta$ with the direction O$x$ (see Fig. 19). The tangent $D(\theta)$ of the curve (Cr) at A is also characterized by $\mathbf{u}$ or by a parallel vector $\mathbf{h}$ that originates from O and ends at the point B of the tangent $D(\theta)$, while $\mathbf{h} \perp D(\theta)$. Vector $\mathbf{h}(\theta)$ related to $\mathbf{r}(\varphi)$ as described above determines the curve (P) – the so-called pedal of (Cr).

One can write down the parametric equation of the curve (Cr) with $h(\theta)$ as (see e.g. in [74])

$$x = h(\theta)\cos\theta - h'(\theta)\sin\theta$$
$$y = h(\theta)\sin\theta + h'(\theta)\cos\theta \ . \tag{A.1}$$

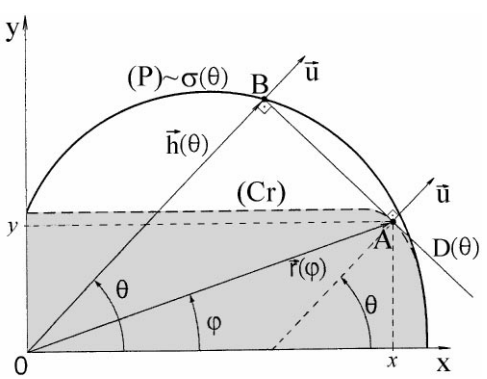


Fig. 19. Illustration of the vectors $\mathbf{r}(\phi)$ and $\mathbf{h}(\theta)$ describing the interface (Cr) and its pedal (P) (proportional to $\sigma(\theta)$), respectively. The gray region represents a quarter of the equilibrium shape shown in Fig. 2(a).

Since $ds = (dx^2 + dy^2)^{1/2} = (x'^2 + y'^2)^{1/2}\,d\theta$, the surface free energy of the crystal is given by

$$F_S = \int_0^{2\pi} \sigma(\theta)(x'^2 + y'^2)^{1/2}\,d\theta\ , \tag{A.2}$$

where $\sigma(\theta)$ is the surface free energy (or surface tension) per unit length of the element $ds$, $x' = dx/d\theta$ and $y' = dy/d\theta$. On the other hand, integrating over the contour (Cr) one can obtain the area $A$ of the crystal

$$A = \frac{1}{2}\oint_{Cr}(x\,dy - y\,dx) = \frac{1}{2}\int(xy' - yx')\,d\theta\ . \tag{A.3}$$

Using (A.1) Eqs. (A.2) and (A.3) become

$$F_S = \int \sigma(\theta)\cdot[h(\theta) + h''(\theta)]\,d\theta\ , \tag{A.4}$$

$$A = \frac{1}{2}\int h(\theta)[h(\theta) + h''(\theta)]\,d\theta\ , \tag{A.5}$$

where $h''(\theta) = (d^2h(\theta)/d\theta^2)$.

For the equilibrium shape with the centre of symmetry in origin O (see Fig. 19) the minimalization of $F_S$ with the constrain of $A = \text{const}$ gives a result (see in [74]):

$$\frac{\sigma(\theta)}{h(\theta)} = \text{const}\ , \tag{A.6}$$

i.e., $\sigma(\theta)$ is proportional to the pedal (P) described by $\mathbf{h}(\theta)$.

Let us consider some singularities of the $\sigma$-plot. First, suppose that the equilibrium shape has a facet (as in Fig. 19). When $\mathbf{r}(\varphi)$ describes this facet, different values of $\varphi$ give the same image $\theta_0$ ($\theta_0 = 90^\circ$ in Fig. 19). In other words, the facet in the equilibrium form has a unique surface tension $\sigma(\theta_0)$ and produces singularity (cusp) in $\sigma(\theta)$ as it is shown in Fig. 19 for $\theta_0 = 90^\circ$.

If the equilibrium form (Cr) has a convex corner at an angle $\varphi_0$ the tangent of the interface is not defined at that point. Consequently, the value of $\sigma(\theta)$ corresponding to the corner in (Cr) cannot be determined uniquely – forbidden directions appear in $\sigma(\theta)$ (for more details see e.g. [74]).

Finally, let us consider a curved part of the convex equilibrium form when $r(\varphi)$ has a maximum at $\varphi_0$. In this case $\theta_0 = \varphi_0$ and $\sigma(\theta_0) = r(\varphi_0)$ (see, e.g. in [74]) and consequently, the function $\sigma(\theta)$ touches the equilibrium form (Cr) of the crystal at $r(\varphi_0)$ – see in Fig. 19 for $\varphi_0 = \theta_0 = 0$.

When a facet appears in the equilibrium shape of the crystal it can be connected with the adjacent, curved part of the phase boundary on two different ways: (I.) tangentially, when there is no discontinuity of the tangents along the equilibrium form, but there is a discontinuity of second order given by the radius of curvature, or (II.) forming a cusp (forbidden directions in $\sigma(\theta)$ – see above). Geometrical construction of the so called critical circle has been proposed in [95] in order to determine the type of the connection – for the more detailed study of the problem see, e.g. [74].

## References


[1] D. Hurle (Ed.), Handbook of Crystal Growth, North-Holland, Amsterdam, 1993.
[2] C. Godrèche (Ed.), Solids Far from Equilibrium, Cambridge University Press, Cambridge, 1991.
[3] J. Langer, Rev. Mod. Phys. 52 (1980) 1.
[4] E. Brener, V. Melnikov, Adv. Phys. 40 (1991) 53.
[5] B. Caroli, C. Caroli, B. Roulet, Instabilities of planar solidification fronts, in: C. Godréche (Ed.), Solids Far from Equilibrium, Cambridge University Press, Cambridge, 1991.
[6] P. Noizères, Shape and growth of crystals, in: C. Godréche (Ed.), Solids Far from Equilibrium, Cambridge University Press, Cambridge, 1991.
[7] K. Koo, R. Ananth, W. Gill, Phys. Rev. A 44 (1991) 3782.
[8] D. Ovsienko, G. Alfintsev, V. Maslov, J. Crystal Growth 26 (1974) 233.
[9] S. Huang, M. Glicksmann, Acta Metallogr. 29 (1981) 701.
[10] J. Bilgram, M. Firmann, E. Huerlimann, J. Crystal Growth 96 (1989) 175.
[11] J. Franck, J. Jung, Physica D 23 (1986) 259.
[12] P. Oswald, F. Melo, C. Germain, J. Phys. (Paris) 50 (1989) 3527.
[13] Á. Buka, N. Éber, Europhys. Lett. 21 (1993) 477.
[14] P. de Gennes, J. Prost, Physics of Liquid Crystals, Clarendon Press, Oxford, 1993.
[15] G. Gray, J. Goodby, Smectic Liquid Crystals, Leonard Hill, Glasgow, London, 1984.
[16] P. Pershan, Structure of Liquid Crystal Phases, World Scientific, Singapore, 1988.
[17] H. Hervet, F. Rondelez, W. Urbach, Transport properties in liquid crystals, in: S. Chandrasekhar (Ed.), Liquid Crystals, Heyden, London, 1980, p. 263.
[18] F. Rondelez, W. Urbach, H. Hervet, Phys. Rev. Lett. 41 (1978) 1058.
[19] U. Zammit, M. Marinelli, R. Pizzoferrato, F. Scudieri, S. Martellucci, Phys. Rev. A 41 (1990) 1153.
[20] W. Urbach, H. Hervet, F. Rondelez, J. Chem. Phys. 78 (1983) 5113.
[21] P. Hohenberg, B. Halperin, Rev. Mod. Phys. 49 (1977) 245.
[22] G.J. Fix, in: A. Fasano, M. Primicerio (Eds.), Free-Boundary Problems: Theory and Applications, Pitman, Boston, 1983.
[23] J.S. Langer, in: G. Grinstein, G. Mazenko (Eds.), Directions in Condensed Matter Physics, World Scientific, Singapore, 1986.
[24] J.B. Collins, H. Levine, Phys. Rev. B 31 (1985) 6119.
[25] G. Caginalp, in: L. Garrido (Ed.), Applications of Field Theory to Statistical Mechanics, Lecture Notes in Physics, Vol. 216, Springer, Berlin, 1985.
[26] G. Caginalp, Arch. Rational Mech. Anal. 92 (1986) 205.
[27] G. Caginalp, Phys. Rev. A 39 (1989) 5887.
[28] M. Gurtin, in: S. Antman, J. Ericksen, D. Kinderlehrer, I. Müller (Eds.), Metastability and Incompletely Posed Problems, Springer, Berlin, 1987.
[29] P. Fife, G. Gill, Physica D 35 (1989) 267.
[30] P. Fife, G. Gill, Phys. Rev. A 43 (1991) 843.
[31] H. Löwen, J. Bechhoefer, L. Tuckerman, Phys. Rev. A 45 (1992) 2399.
[32] O. Penrose, P.C. Fife, Physica D 43 (1990) 44.
[33] O. Penrose, P.C. Fife, Physica D 69 (1993) 107.
[34] P.W. Bates, P.C. Fife, R.A. Gardner, C.K.R.T. Jones, Physica D 104 (1997) 1.
[35] J.-T. Lin, SIAM J. Numer. Anal. 25 (1988) 1015.
[36] S. Schofield, D. Oxtoby, J. Chem. Phys. 94 (1991) 2176.
[37] G. Caginalp, E. Socolovsky, J. Comput. Phys. 95 (1991) 85.
[38] R. Kobayashi, Bull. Jpn. Soc. Ind. Appl. Math. 1 (1991) 22.
[39] R. Kobayashi, Physica D 63 (1993) 410.
[40] R. Kobayashi, in: S. Kai (Ed.), Pattern Formation in Complex Dissipative Systems, World Scientific, Singapore, 1992.
[41] R. Kobayashi, Exp. Math. 3 (1994) 59.

[42] A.A. Wheeler, W.J. Boettinger, G.B. McFadden, Phys. Rev. A 45 (1992) 7424.
[43] S.-L. Wang, R.F. Sekerka, A.A. Wheeler, B.T. Murray, S.R. Coriell, R.J. Braun, G.B. McFadden, Physica D 69 (1993) 189.
[44] G.B. McFadden, A.A. Wheeler, R.J. Braun, S.R. Coriell, R.F. Sekerka, Phys. Rev. E 48 (1993) 2016.
[45] A.A. Wheeler, B.T. Murray, R.J. Schaefer, Physica D 66 (1993) 243.
[46] A.A. Wheeler, W.J. Boettinger, G.B. McFadden, Phys. Rev. E 47 (1993) 1893.
[47] R.J. Braun, G.B. McFadden, Phys. Rev. E 49 (1994) 4336.
[48] K.R. Elder, F. Drolet, J.M. Kosterlitz, M. Grant, Phys. Rev. Lett. 72 (1994) 677.
[49] B.T. Murray, A.A. Wheeler, M.E. Glicksman, J. Crystal Growth 154 (1995) 386.
[50] S.-L. Wang, R.F. Sekerka, Phys. Rev. E 53 (1996) 3760.
[51] M. Conti, Phys. Rev. E 56 (1997) 3197.
[52] R. González-Cinca, L. Ramirez-Piscina, J. Casademunt, A. Hernández-Machado, L. Kramer, T. Tóth-Katona, T. Börzsönyi, Á. Buka, Physica D 99 (1996) 359.
[53] T. Tóth-Katona, T. Börzsönyi, Z. Váradi, J. Szabon, Á. Buka, R. González-Cinca, L. Ramirez-Piscina, J. Casademunt, A. Hernández-Machado, Phys. Rev. E 54 (1996) 1574.
[54] R. González-Cinca, L. Ramirez-Piscina, J. Casademunt, A. Hernández-Machado, T. Tóth-Katona, T. Börzsönyi, Á. Buka, J. Crystal Growth 193 (1998) 712.
[55] A. Karma, W.-J. Rappel, Phys. Rev. E 53 (1996) 3017.
[56] A. Karma, W.-J. Rappel, Phys. Rev. Lett. 77 (1996) 4050.
[57] A. Karma, W.-J. Rappel, Phys. Rev. E 57 (1998) 4323.
[58] A. Bösch, H. Müller-Krumbhaar, O. Shochet, Z. Physik B 97 (1995) 367.
[59] R.J. Braun, B.T. Murray, J. Crystal Growth 174 (1997) 41.
[60] N. Provatas, N. Goldenfeld, J. Dantzig, Phys. Rev. Lett. 80 (1998) 3308.
[61] L. Sallen, P. Oswald, J. Gèminard, J. Malthete, J. Phys. II. France 5 (1995) 937.
[62] G. Wulff, Z. Kristallogr. Mineral. 34 (1901) 449.
[63] Á. Buka, T. Tóth-Katona, L. Kramer, Phys. Rev. E 49 (1994) 5271.
[64] T. Börzsönyi, A. Buka, L. Kramer, Phys. Rev. E 58 (1998) 3236.
[65] T. Tóth Katona, Á. Buka, Mol. Cryst. Liq. Cryst. 261 (1995) 349.
[66] T. Tóth-Katona, Ph.D. Thesis, University Eötvös Loránd, Budapest, 1998.
[67] M. Muschol, D. Liu, H. Cummins, Phys. Rev. A 46 (1992) 1038.
[68] M. Glicksmann, N. Singh, J. Crystal Growth 98 (1989) 277.
[69] A. Dougherty, J. Crystal Growth 110 (1991) 501.
[70] E. Rubinstein, M. Glicksman, J. Crystal Growth 112 (1991) 97.
[71] J. Géminard, P. Oswald, Phys. Rev. E 55 (1997) 4442.
[72] Á. Buka, T. Tóth-Katona, L. Kramer, Phys. Rev. E 51 (1995) 571.
[73] R. Brownsey, A. Leadbetter, J. Phys. Lett. 42 (1981) 135.
[74] R. Kern, The equilibrium form of a crystal, in: I. Sunagawa (Ed.), Morphology of Crystals, Terra Scientific Publishing Company, Tokyo, 1987.
[75] P. Oswald, J. Phys. (Paris) 49 (1988) 2119.
[76] P. Oswald, J. Malthéte, P. Pelcé, J. Phys. 50 (1989) 2121.
[77] J. Géminard, P. Oswald, D. Temkin, J. Malthête, Europhys. Lett. 22 (1993) 69.
[78] E. Ben-Jacob, P. Garik, Physica D 38 (1989) 16.
[79] E. Ben-Jacob, P. Garik, Nature 343 (1990) 523.
[80] E. Brener, H. Müller-Krumbhaar, D. Temkin, Europhys. Lett. 17 (1992) 535.
[81] T. Tóth-Katona, T. Börzsönyi, Á. Buka, Mol. Cryst. Liq. Cryst. 339 (2000) 175.
[82] T. Börzsönyi, Ph.D. Thesis, University Eötvös Loránd, Budapest, 1998.
[83] M. Marinelli, private communication.
[84] S. Chandrasekhar, in: Liquid Crystals, Cambridge University Press, Cambridge, 1992.
[85] M. Wortis, Fundamental problems in statistical mechanics VI, in: E. Cohen (Ed.), Proceedings of the 1984 Trondheim Summer School, North-Holland, Amsterdam, 1985, p. 87.

[86] H. van Beijeren, I. Nolden, in: W. Schommers, P. van Blankenhagen (Eds.), Structure and Dynamics of Surfaces II, Springer, Berlin, 1987, p. 259.
[87] P. Oswald, F. Melo, J. Phys. II (France) 2 (1992) 1345.
[88] E. Raz, S. Lipson, E. Polturak, Phys. Rev. A 40 (1989) 1088.
[89] X. Qian, H.Z. Cummins, Phys. Rev. Lett. 64 (1990) 3038.
[90] L. Williams, M. Muschol, X. Qian, W. Losert, H.Z. Cummins, Phys. Rev. E 48 (1993) 489.
[91] B.T. Murray, A.A. Wheeler, M.E. Glicksman, J. Crystal Growth 154 (1995) 386.
[92] Ph. Bouissou, A. Chiffaudel, B. Perrin, P. Tabeling, Europhys. Lett. 13 (1990) 89.
[93] T. Börzsönyi, T. Tóth-Katona, Á. Buka, L. Gránásy, Phys. Rev. Lett. 83 (1999) 2853.
[94] A.G. Notcovich, I. Braslavsky, S.G. Lipson, J. Crystal Growth 198/199 (1999) 10.
[95] C. Herring, The use of classical macroscopic concepts in surface energy problems, in: R. Gomer, C.S. Smith (Eds.), Structures and Properties of Solid Surfaces, University of Chicago Press, Chicago, 1953.